

Research Article

Effects of Substrate Temperature on the Corrosion Behaviour of Nanochromium Coatings Deposited by Direct Current Magnetron Sputtering

Yanjie Ren, Jian Chen, Yaqing Chen, Jianlin Chen, and Wei Qiu

Department of Energy and Power Engineering, Changsha University of Science and Technology, Changsha 410076, China

Correspondence should be addressed to Yanjie Ren; yjren1008@163.com

Received 17 April 2016; Accepted 16 May 2016

Academic Editor: Lihui Liu

Copyright © 2016 Yanjie Ren et al. This is an open access article distributed under the Creative Commons Attribution License, which permits unrestricted use, distribution, and reproduction in any medium, provided the original work is properly cited.

Nanochromium coatings were deposited on 316L stainless steel bipolar plates of a proton-exchange membrane fuel cell (PEMFC) by a direct current magnetron sputtering technique. The effect of substrate temperature on the corrosion resistance of nanochromium coatings was investigated. The corrosion performance of the bare and chromium-coated steel in a simulated environment of PEMFC ($0.5\text{ M H}_2\text{SO}_4 + 2\text{ ppm F}^-$) was studied using electrochemical impedance spectroscopy, polarisation, and open circuit potential measurements. The results showed that the corrosion rates of two nanochromium coatings deposited at 300°C and 500°C were lower than those of uncoated steel by more than one order of magnitude. Electrochemical impedance spectra of both nanochromium coatings exhibited distinct characteristics in corrosive solution. The nanochromium coating deposited at 500°C showed superior stability in the corrosive solution.

1. Introduction

The proton-exchange membrane fuel cell (PEMFC) is a promising power generation system that converts energy, with water as the only by-product. The bipolar plate is a critical component of the PEMFC that conducts current between cells, facilitates water and thermal management through the cell, and distributes and separates the cathodic and anodic reactant gases. The main materials used for bipolar plates include graphite, metal, and graphite polymer composites. Graphite and graphite composites are the most commonly used bipolar plate materials due to their low surface contact resistance and high chemical stability. Unfortunately, graphite is too brittle to be machined to form thin plates with gas channels on each side, and it has relatively high gas permeability, which lowers the power density of the fuel cell stack. Metallic bipolar plates possess high electrical conductivity, acceptable material cost, high strength, and low gas permeability. Moreover, metallic materials could significantly reduce the volume and weight of a PEMFC [1]. The main problems associated with metallic materials are their inability to resist corrosion in a weakly acidic medium inside

the PEMFC and the formation of passive films and metal ions. The formation of passive films increases the contact resistance, while the dissolution of metals contaminates the membrane electrodes [2]. To solve this problem, various protective coatings with high electrical conductivities have been proposed to protect the metallic bipolar plates to achieve high corrosion resistance and low contact resistance [3–9].

Chromium coating has frequently been used in the surface treatment of metals and alloys. It is accepted that both chromium itself and chromium coatings possess excellent corrosion resistance due to the formation of a passive film. It has been reported that nanocrystallisation of inactive metals and films could form a distinct passive film as a result of its different nucleation and growth process, which correlates with the corrosion behaviour and conductivity of coatings [10]. The characters of nanochromium coatings on the metallic bipolar plates have not yet been reported.

Chromium coatings are usually deposited on a substrate by either chemical or electrochemical methods. However, these approaches make use of toxic reactants and produce toxic waste products and pollutants. In addition, microcracks are formed during electrodeposition due to adsorbed

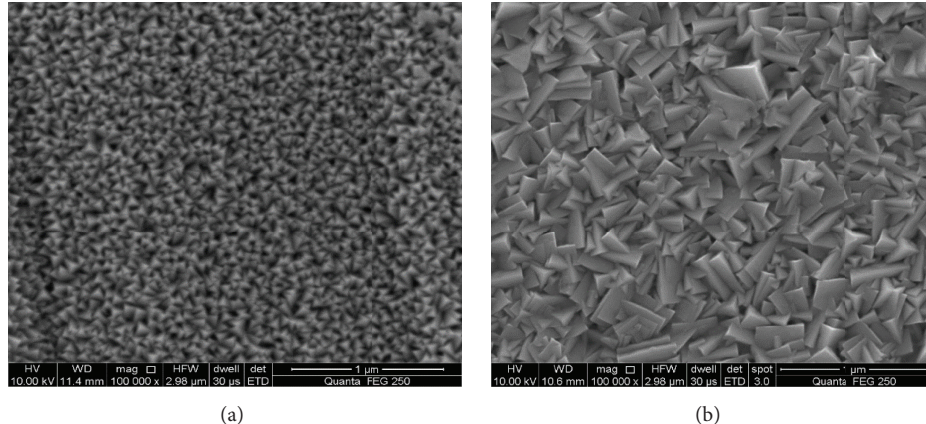


FIGURE 1: Surface morphology of nanochromium coatings deposited by magnetron sputtering with substrate temperatures (a) 300°C and (b) 500°C.

hydrogen atoms [11, 12]. Magnetron sputtering is an effective technique for depositing coatings because it allows for easy control of the composition, crystal structure, and stoichiometry of each layer. It has therefore been widely used for the deposition of corrosion-resistant, wear-resistant, and electrically insulating coatings and for decorative coatings on workpieces [13, 14].

In this study, we focused on the effect of substrate temperature on the corrosion behaviour of nanoscale chromium coatings on 316L stainless steel bipolar plates of a PEMFC. The deposited films were characterized by scanning electron microscopy (SEM) and X-ray diffraction (XRD). The corrosion resistance of the chromium films was investigated by potentiodynamic polarisation measurements and electrochemical impedance spectroscopy (EIS).

2. Experimental Methods

2.1. Preparation of Nanochromium Coatings. 316L stainless steel was used as the substrate alloy. The steel plates were cut into specimens of 20 × 20 mm, followed by grinding with 1000-grit silicon carbide (SiC) paper and degreasing with acetone ((CH₃)₂CO). A multitarget reactive DC magnetron sputtering system (JZCK-450, Intelligence-Gathering Vacuum Equipment Co., Ltd., China) was employed and a base vacuum pressure of 8.0 × 10⁻³ Pa was used. Chromium target coverage of 99.99% at room temperature (RT) was used and an interelectrode distance was 10 cm. The ion current density was 0.35 A. The substrate temperatures were 300°C and 500°C. The sputtering time was 2 h. Scanning electron microscopy (SEM) and X-ray diffraction (XRD) were employed to characterize the coatings. Jade 5.0 software was used to evaluate the grain size of the chromium films.

2.2. Electrochemical Measurements. A conventional three-electrode system was used for the electrochemical measurements, with a platinum sheet as the counter electrode and a saturated calomel electrode (SCE) as the reference electrode. All electrochemical measurements were carried out in 0.5 M H₂SO₄ + 2 ppm F⁻ solution at RT with a

Zahner Zennium Potentiostat/Galvanostat. Potentiodynamic polarisation measurements used a scan rate of 20 mV min⁻¹ following immersion for 1 h in 0.5 M H₂SO₄ + 2 ppm F⁻ solution. Electrochemical impedance measurements were carried out in the range 0.01–100 kHz at open circuit potential (OCP). The amplitude of the input sine wave voltage was 5 mV.

3. Results and Discussion

3.1. Morphology and Microstructure. Figure 1 shows the surface morphology of chromium coatings deposited at 300°C (named Cr-1) and 500°C (named Cr-2), but otherwise with identical deposition parameters, as mentioned in Section 2. The specimens having the Cr-1 coating exhibited a three-dimensional island structure with an open boundary (Figure 1(a)), with an average grain size of about 50 nm. It was observed that obvious defects existed within it. In contrast, the Cr-2 coating exhibited a compact pyramidal structure with a variable grain size that was larger than that of the Cr-1 specimens (as shown in Figure 1(b)). The nucleation and growth of as-deposited films are thermodynamic nonequilibrium processes. As the substrate temperature is low, the critical nucleation free energy is low, which results in a smaller grain dimension of as-deposited coating. When the substrate temperature increases, the grain dimension also increases due to the higher critical nucleation free energy [15]. In contrast, at low substrate temperatures the atoms diffuse with difficulty and produce shadow effects, which contribute to the columnar structure of the coatings [16]. However, at high substrate temperatures the sputtered atoms diffuse easily and the self-shadow effect is avoided. It was observed that the Cr-2 coating showed a more compact structure.

The XRD patterns of chromium films deposited at 300°C and 500°C are shown in Figure 2. Cr (110) and Cr (211) peaks can be seen clearly. An additional Cr (200) peak appeared for Cr-2 coating.

3.2. Electrochemical Polarisation Measurements. Figure 3 shows the potentiodynamic polarisation curves for bare steel and for chromium coatings in 0.5 M H₂SO₄ + 2 ppm F⁻

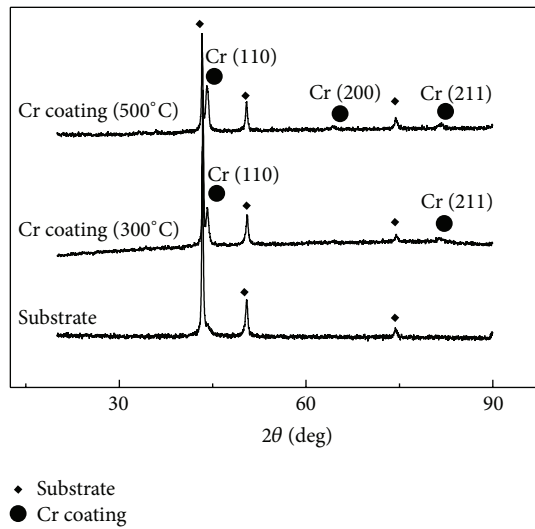


FIGURE 2: XRD patterns of chromium films with substrate temperatures 300°C and 500°C by magnetron sputtering.

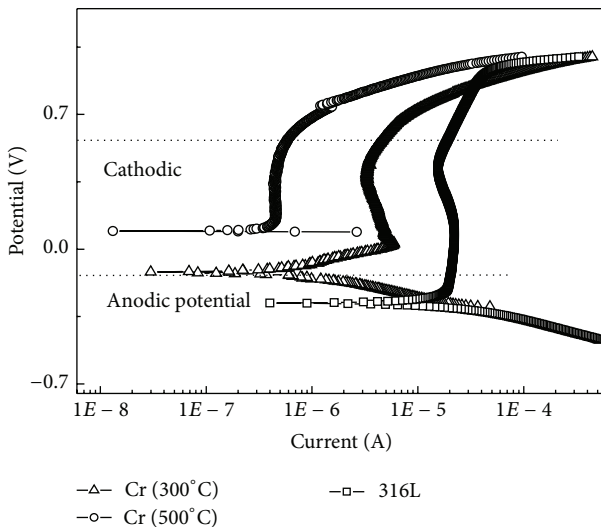


FIGURE 3: Potentiodynamic polarisation curves for 316L stainless steel and nanochromium coatings in 0.5 M H_2SO_4 + 2 ppm F^- solution.

solution at room temperature, respectively. Both the Cr-2 coating and the 316L stainless steel were in a passive state at the corrosion potential (E_{corr}). The chromium coatings deposited at 300°C were in an active state at E_{corr} at -119 mV SCE. The increased current density of the Cr-1 coating is related to its smaller grain size and open structure, which enlarged the exposed area to the corrosive solution. E_{corr} and the corrosion current density (I_{corr}) for 316L stainless steel were -289 mV SCE and $20.1 \mu\text{A cm}^{-2}$, respectively. E_{corr} and I_{corr} for the Cr-1 coating were -119 mV SCE and $1.27 \mu\text{A cm}^{-2}$, while for the Cr-2 coating with a compact structure they were 96 mV SCE and $0.35 \mu\text{A cm}^{-2}$, respectively.

The cathode operation potential at 0.6 V SCE was marked by the dotted line and the passivation current density of

316L stainless steel at the cathode operation potential was $19.5 \mu\text{A cm}^{-2}$. In contrast, the current densities of the Cr-1 and Cr-2 coatings were significantly reduced to $4.83 \mu\text{A cm}^{-2}$ and $0.59 \mu\text{A cm}^{-2}$, respectively. The smaller anodic current density usually implied better durability and a lower corrosion rate. The anode potential (-0.1 V SCE) was in the active region of 316L stainless steel and the Cr-1 coating, and the current densities were $19.8 \mu\text{A cm}^{-2}$ and $0.41 \mu\text{A cm}^{-2}$, respectively, but the corrosion potential of the Cr-2 coating shifted towards the positive direction, reaching about 96 mV SCE. This was more positive than the operating potential in the PEMFC anode environment. Hence, the anode operation potential was cathodic to Cr-2 and corrosion was retarded.

3.3. Open Circuit Potential Measurements. The high stability of nanochromium coatings in $0.5 \text{ M } \text{H}_2\text{SO}_4 + 2 \text{ ppm } \text{F}^-$ solution was also demonstrated by the measurements of open circuit potential versus time curves for chromium-coated and the bare steel, as shown in Figures 4(a) and 4(b), respectively. For 316L, E_{oCP} was maintained at about -250 mV SCE in corrosive solution (Figure 4(a)). As shown in Figure 4(b), E_{oCP} for Cr-1 coatings increased to 278 mV SCE during immersion for 264 h in corrosive solution and then decreased gradually. For the Cr-2 coating, E_{oCP} increased after immersion for 768 h and its potential remained at about 400 mV SCE. As a passive layer developed, the OCP of Cr-2 coatings increased and remained stable. The OCP was higher than that reported in the literature [12], which was related to nanostructures of the coating. The corrosion resistance of the chromium coating deposited at 300°C shows inferior stability due to its open structure, compared with that deposited at 500°C.

3.4. Electrochemical Impedance Measurements. Figure 5 showed the typical Nyquist and Bode plots for the corrosion of 316L stainless steel in $0.5 \text{ M } \text{H}_2\text{SO}_4 + 2 \text{ ppm } \text{F}^-$ solution after various exposure times. The Nyquist plots were composed of two depressed semicircles. An equivalent circuit of Figure 6 was proposed to fit the impedance plots. R_s was the electrolyte resistance. R_f and C_f represented, respectively, the resistance and capacitance of the porous corrosion products formed on the alloy surface. R_t and C_{dl} were the charge transfer resistance and double-layer capacitance, respectively. A constant phase element (CPE) was used in the fitting procedures. Table 1 gives the fitted results of impedance spectra for the corrosion of 316L stainless steel. It could be observed that the values of R_t tend to increase with exposure time, suggesting a decreased corrosion rate.

Differing from the bare steel, the impedance spectra of Cr-1 coating exhibit different characters in the corrosive solution. After immersion for 1 h, the Nyquist plots consist of two capacitive loops, as shown in Figure 7(a), which were correlated with an incomplete chromium oxide film. With extended immersion time, the Nyquist plots consist of a small capacitive loop in the high-frequency region and a nearly vertical line at low frequency, as shown in Figure 7(b). The Bode diagrams show a large frequency region of the maximum phase angle, with values greater than 85° , close to the 90° value, which are characteristic of a predominantly

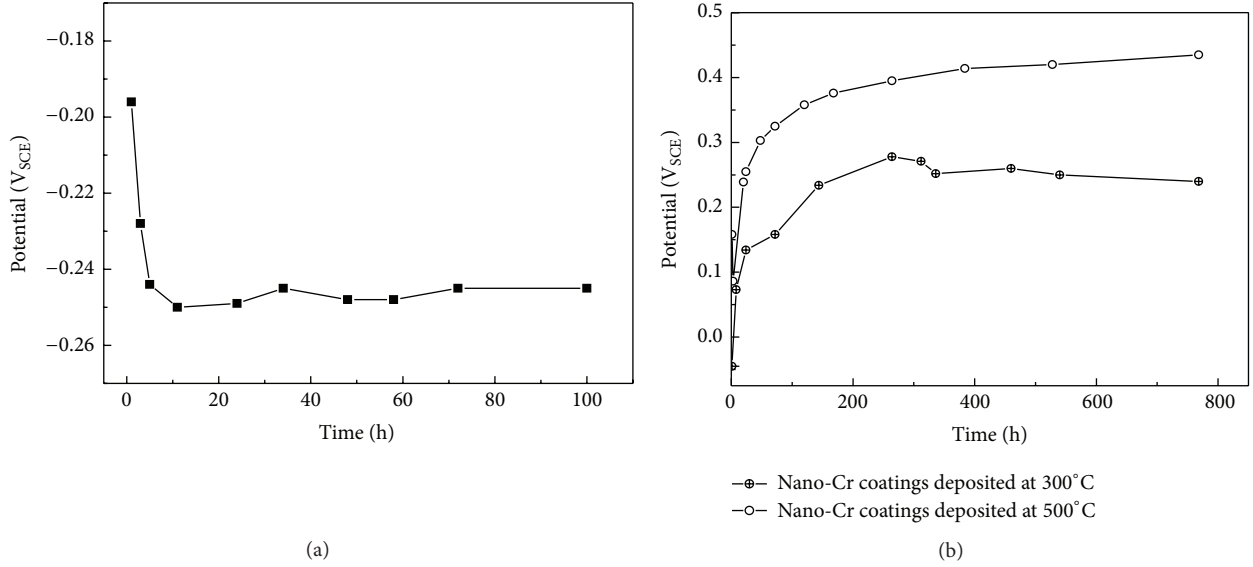


FIGURE 4: Open circuit potential-time curves for (a) 316L and (b) nano-Cr-1 and nano-Cr-2 coatings in 0.5 M H₂SO₄ + 2 ppm F⁻ solution.

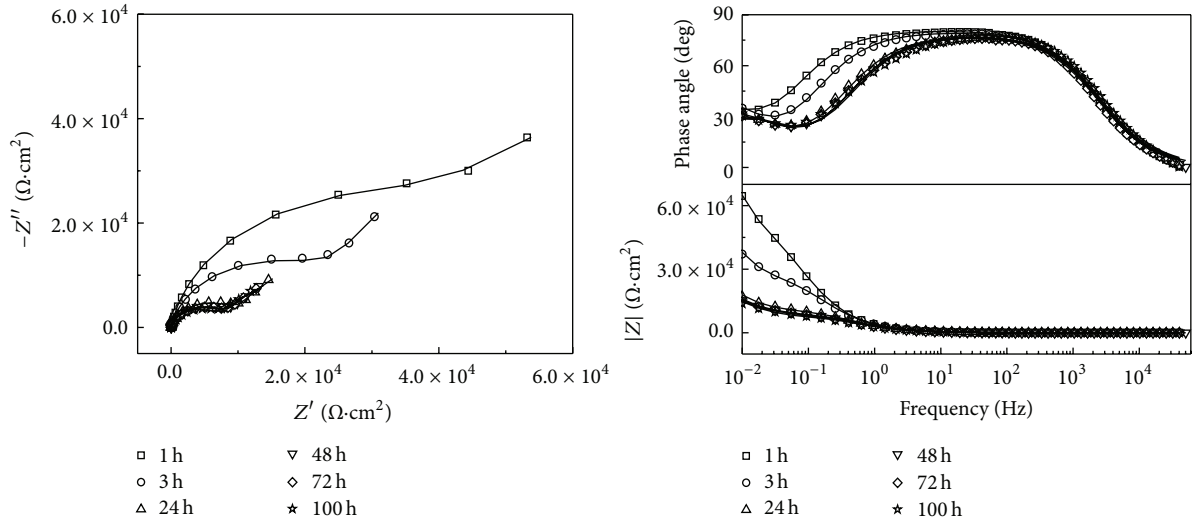


FIGURE 5: Nyquist and Bode plots for 316L after various exposure times at open circuit potential in 0.5 M H₂SO₄ + 2 ppm F⁻ solution. Symbols: experimental data; line: fitted data.

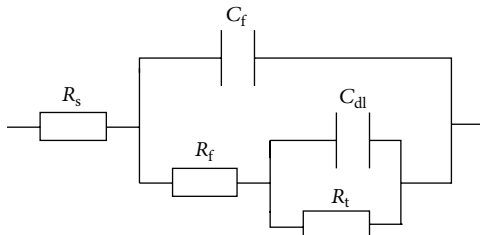


FIGURE 6: Equivalent circuit representing the corrosion of 316L in 0.5 M H₂SO₄ + 2 ppm F⁻ solution.

capacitive behaviour. For some anodised valve metals (such as Ti, Bi, and Al), EIS show similar characteristics in the

initial period of oxide film formation in aqueous solution [17, 18]. However, previous studies have not reported similar results for chromium or other inactive films containing a developed passive film. Since the passive film formation is mainly determined by nucleation and growth processes, defects, dislocations, grain boundaries, and grain boundary junctions generate nucleation of passive films [19]. Compared to coarse-grained structures, nanocrystalline materials are composed of a large fraction of surface defects which alter the nucleation mechanism of passive films from progressive to instantaneous. Passive films are composed of multilayers, investigated by a potentiostatic-galvanostatic (P-G) transient technique, which are different from those grown on coarse-grained materials [20].

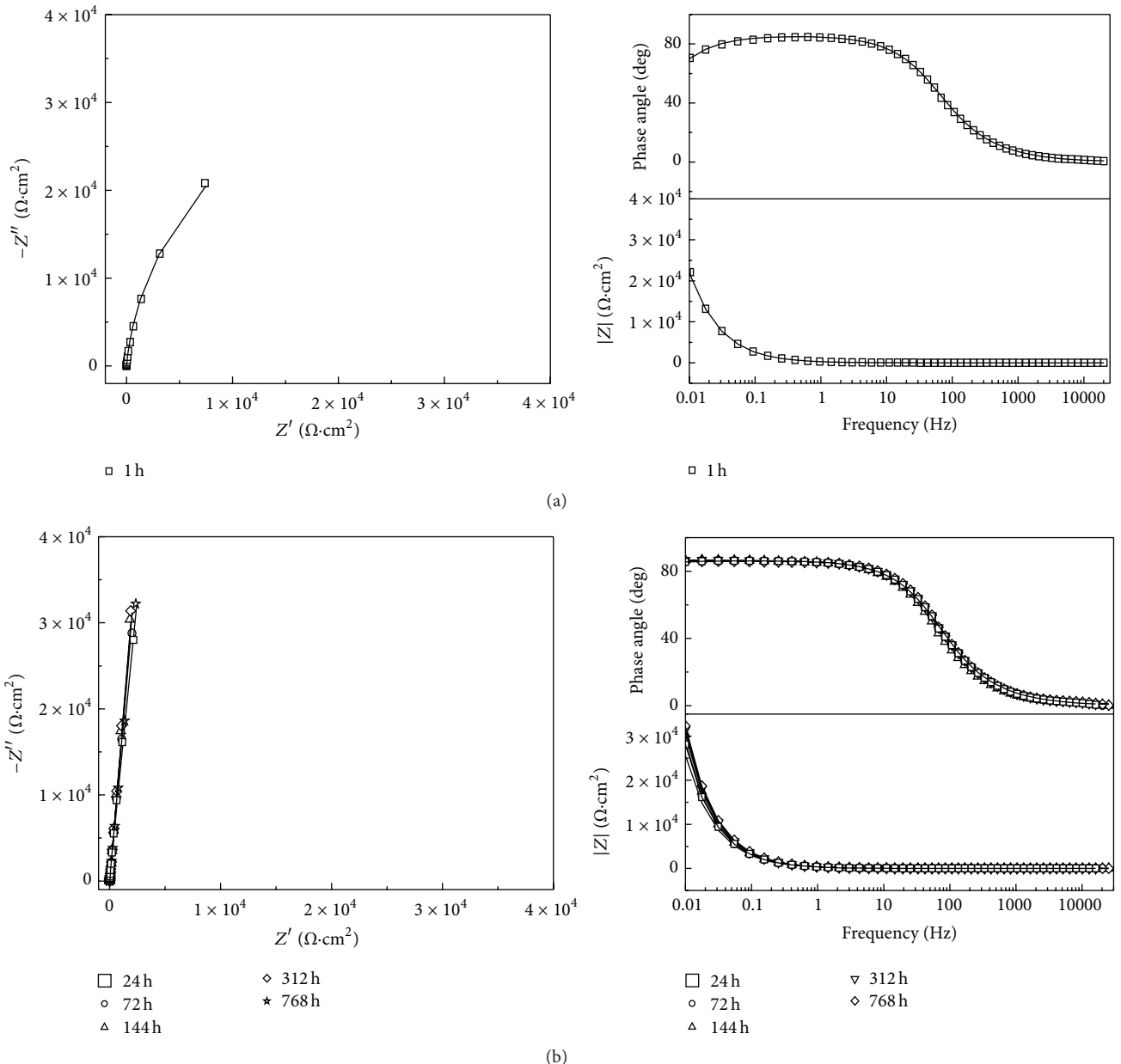


FIGURE 7: Nyquist and Bode plots for nanochromium coatings with substrate temperature 300°C after various exposure times at open circuit potential in 0.5 M H₂SO₄ + 2 ppm F⁻ solution. Symbols: experimental data; line: fitted data.

TABLE 1: Fitting results of impedance spectra for the corrosion of 316L stainless steel in 0.5 M H₂SO₄ + 2 ppm F⁻ solution.

Time (h)	R_s ($\Omega \cdot \text{cm}^2$)	Y_f ($\Omega^{-1} \cdot \text{cm}^{-2} \text{S}^{-n}$)	n_f	R_f ($\Omega \cdot \text{cm}^2$)	Y_{dl} ($\Omega \cdot \text{cm}^2 \text{S}^{-n}$)	n_{dl}	R_t ($\Omega \cdot \text{cm}^2$)
1	2.041	$8.164E - 5$	0.850	0.033	$1.583E - 5$	0.992	$1.490E4$
3	1.835	$8.427E - 5$	0.838	0.039	$1.548E - 5$	0.865	$9.420E3$
24	1.982	$2.758E - 5$	0.978	5.070	$9.695E - 5$	0.748	$6.272E3$
100	1.683	$3.126E - 5$	0.912	6.084	$1.080E - 4$	0.733	$4.441E3$

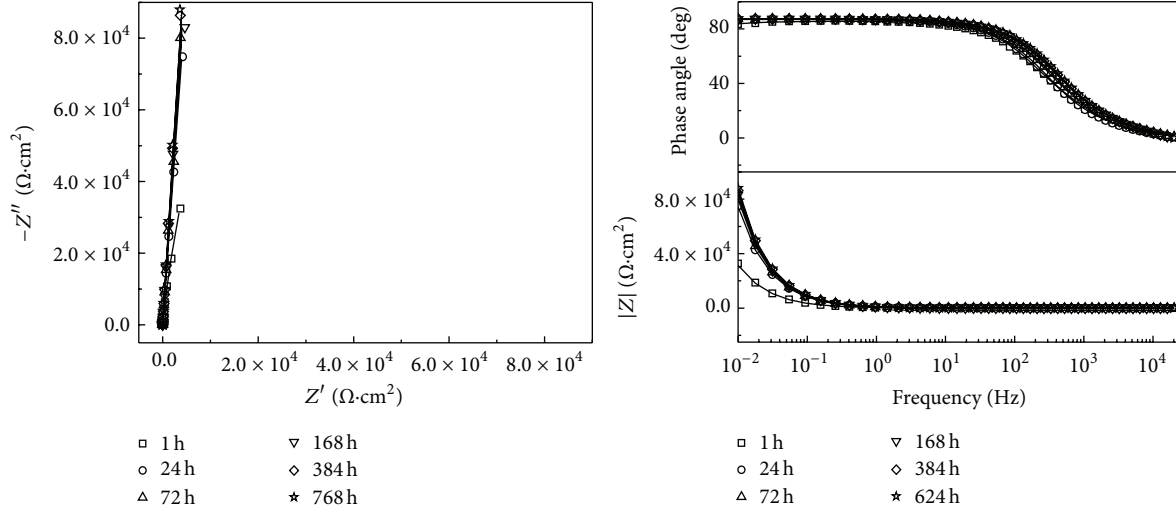


FIGURE 8: Nyquist and Bode plots for nanochromium coatings with substrate temperature 500°C after various exposure times at open circuit potential in 0.5 M H₂SO₄ + 2 ppm F⁻ solution. Symbols: experimental data; line: fitted data.

TABLE 2: Fitting results of impedance spectra for the corrosion of Cr-1 coatings in 0.5 M H₂SO₄ + 2 ppm F⁻ solution.

Time (h)	R_s ($\Omega \cdot \text{cm}^2$)	Y_f ($\Omega^{-1} \cdot \text{cm}^{-2} \text{S}^{-n}$)	n_f	R_f ($\Omega \cdot \text{cm}^2$)	Y_{dl} ($\Omega \cdot \text{cm}^2 \text{S}^{-n}$)	n_{dl}	R_t ($\Omega \cdot \text{cm}^2$)
1	2.191	6.605E - 4	0.958	1.348	5.488E - 4	0.944	4.063E4
24	2.274	4.905E - 4	0.969	1.141	5.229E - 4	0.946	—
72	2.385	4.612E - 4	0.967	1.030	5.346E - 4	0.950	—
144	2.728	3.997E - 4	0.965	0.937	5.435E - 4	0.953	—
312	2.499	3.891E - 4	0.967	0.986	5.18E - 4	0.951	—
768	2.546	2.557E - 4	0.963	0.671	6.158E - 4	0.945	—

TABLE 3: Fitting results of impedance spectra for the corrosion of Cr-2 coatings in 0.5 M H₂SO₄ + 2 ppm F⁻ solution.

Time (h)	R_s ($\Omega \cdot \text{cm}^2$)	Y_f ($\Omega^{-1} \cdot \text{cm}^{-2} \text{S}^{-n}$)	n_f	R_f ($\Omega \cdot \text{cm}^2$)	Y_d ($\Omega^{-1} \cdot \text{cm}^{-2} \text{S}^{-n}$)	n_d
1	1.501	2.796E - 4	0.962	2.606	1.647E - 4	0.936
72	1.307	2.291E - 4	0.974	2.414	1.378E - 4	0.952
168	1.174	2.220E - 4	0.979	2.903	1.309E - 4	0.951
384	1.174	2.212E - 4	0.978	2.490	1.209E - 4	0.952
768	1.162	2.266E - 4	0.976	2.662	1.097E - 4	0.954

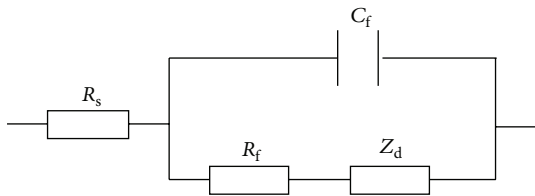


FIGURE 9: Equivalent circuit representing the corrosion of nanochromium coatings in 0.5 M H₂SO₄ + 2 ppm F⁻ solution.

For the Cr-2 coating, the EIS consist of a small capacitive loop in the high-frequency region and a nearly vertical line at low frequency during the initial stage and maintain the same character for the total period of immersion. The impedance diagrams for initial immersion (1 h) of coatings at 300°C can be fitted by the equivalent circuit shown in Figure 6. The

subsequent diagrams and those of the coatings formed at 500°C can be represented by the equivalent circuit shown in Figure 9, where C_f represents the film capacitance, R_f is the resistance of the chromium film, and Z_d is the diffusion impedance of migrating chromium ions along the passive film. Figures 7 and 8 show that there is a close fit for the EIS spectra of nanochromium-coated steel in 0.5 M H₂SO₄ + 2 ppm F⁻ solution. Some electrochemical parameters are given in Tables 2 and 3.

The values of R_f for the Cr-1 coating decreased from 1.348 $\Omega \cdot \text{cm}^2$ to 0.671 $\Omega \cdot \text{cm}^2$ up to 768 h. However, the values of R_f of the Cr-2 coating remained stable with some fluctuation, indicating that the Cr-2 coating retained high chemical stability in solution. The values of n_f related to surface roughness and the distribution of corrosion current on the electrode were close to 1 and almost remained constant, suggesting that a stable, passive film was formed for Cr-2 coatings.

4. Conclusions

The effects of substrate temperature on the corrosion behaviour of nanochromium coatings on 316L stainless steel bipolar plates of a proton-exchange membrane fuel cell were evaluated. The chromium film deposited at 300°C presented a three-dimensional island structure, with an average grain size about 50 nm and containing obvious pores. However, the microstructure of the chromium film deposited at 500°C was dense, with an increasing grain size. In 0.5 M H₂SO₄ + 2 ppm F⁻ solution, the nanochromium coatings deposited at 300°C and 500°C significantly increased the free corrosion potential of the steel, and its corrosion current density was one or two orders of magnitude lower than that of the bare steel. The nanochromium coatings offer excellent corrosion protection for 316L stainless steel in simulated PEMFC environments. In contrast, the chromium coatings deposited with substrate temperature 500°C exhibited superior stability to that obtained with substrate temperature 300°C.

The ongoing research work includes the contact electric resistance and the corrosion resistance of nanochromium coatings in actual PEMFC conditions.

Competing Interests

The authors declare that they have no competing interests.

Acknowledgments

This project was supported by the National Natural Science Foundation of China (Grant no. 51301026), Natural Science Foundation of Hunan Province (Grant no. 14JJ6019), and the Educational Commission of Hunan Province (Grant no. 13B128).

References

- [1] H. Tsuchiya and O. Kobayashi, "Mass production cost of PEM fuel cell by learning curve," *International Journal of Hydrogen Energy*, vol. 29, no. 10, pp. 985–990, 2004.
- [2] A. E. Fetohi, R. M. Abdel Hameed, K. M. El-Khatib, and E. R. Souaya, "Study of different aluminum alloy substrates coated with Ni-Co-P as metallic bipolar plates for PEM fuel cell applications," *International Journal of Hydrogen Energy*, vol. 37, no. 14, pp. 10807–10817, 2012.
- [3] H. L. Wang and J. A. Turner, "Electrochemical nitridation of a stainless steel for PEMFC bipolar plates," *International Journal of Hydrogen Energy*, vol. 36, no. 20, pp. 13008–13013, 2011.
- [4] E. M. Gabreab, G. Hinds, S. Fearn et al., "An electrochemical treatment to improve corrosion and contact resistance of stainless steel bipolar plates used in polymer electrolyte fuel cells," *Journal of Power Sources*, vol. 245, pp. 1014–1026, 2014.
- [5] M. C. Li, S. Z. Luo, C. Zeng, J. Shen, H. Lin, and C. Cao, "Corrosion behavior of TiN coated type 316 stainless steel in simulated PEMFC environments," *Corrosion Science*, vol. 46, no. 6, pp. 1369–1380, 2004.
- [6] D. W. DeBerry, "Modification of the electrochemical and corrosion behavior of stainless steels with an electroactive coating," *Journal of the Electrochemical Society*, vol. 132, no. 5, pp. 1022–1026, 1985.
- [7] D. O. Flamini and S. B. Saidman, "Electrodeposition of polypyrrole onto NiTi and the corrosion behaviour of the coated alloy," *Corrosion Science*, vol. 52, no. 1, pp. 229–234, 2010.
- [8] L. M. Martins dos Santos, J. C. Lacroix, K. I. Chane-Ching, A. Adenier, L. M. Abrantes, and P. C. Lacaze, "Electrochemical synthesis of polypyrrole films on copper electrodes in acidic and neutral aqueous media," *Journal of Electroanalytical Chemistry*, vol. 587, no. 1, pp. 67–78, 2006.
- [9] K. Qi, Y. B. Qiu, Z. Y. Chen, and X. P. Guo, "Corrosion of conductive polypyrrole: Galvanic interactions between polypyrrole and metal substrates," *Corrosion Science*, vol. 91, pp. 272–280, 2015.
- [10] G. Ćirić-Marjanović, "Recent advances in polyaniline research: polymerization mechanisms, structural aspects, properties and applications," *Synthetic Metals*, vol. 177, pp. 1–47, 2013.
- [11] A. Lozano-Morales, R. P. Renz, J. J. Fortman, and E. J. Taylor, "Electrically mediated process for functional and decorative trivalent chromium electroplating: an alternative to hexavalent chromium," *ECS Transactions*, vol. 6, pp. 51–61, 2007.
- [12] Z. X. Zeng and J. Y. Zhang, "Electrodeposition and tribological behavior of amorphous chromium-alumina composite coatings," *Surface and Coatings Technology*, vol. 202, no. 12, pp. 2725–2730, 2008.
- [13] D. Rosestolato, G. Battaglin, and S. Ferro, "Electrochemical properties of stoichiometric RuN film prepared by rf-magnetron sputtering: a preliminary study," *Electrochemistry Communications*, vol. 49, pp. 9–13, 2014.
- [14] K. Nygren, M. Samuelsson, A. Flink, H. Ljungcrantz, Å. K. Rudolphi, and U. Jansson, "Growth and characterization of chromium carbide films deposited by high rate reactive magnetron sputtering for electrical contact applications," *Surface and Coatings Technology*, vol. 260, pp. 326–334, 2014.
- [15] D. B. Lewis, Q. Luo, P. E. Hovsepian, and W.-D. Münz, "Interrelationship between atomic species, bias voltage, texture and microstructure of nano-scale multilayers," *Surface and Coatings Technology*, vol. 184, no. 2–3, pp. 225–232, 2004.
- [16] D. Lan, Y. Wang, and Z. Q. Cao, "Studies on the corrosion electrochemical behavior of nanocrystalline Cr in acidic media," *Journal of Liaoning Technology University*, vol. 31, pp. 387–391, 2012.
- [17] A.-C. Manea, M. Buda, and T. Vişan, "Electrochemical impedance spectroscopy investigations of tantalum and its passive films in some acidic solutions," *UPB Scientific Bulletin, Series B: Chemistry and Materials Science*, vol. 72, no. 4, pp. 65–78, 2010.
- [18] T. D. Radjabov, A. I. Kamardin, and A. V. Sharudo, "The investigation of two-layer protective-decorative coatings on oxide substrates," *Vacuum*, vol. 75, no. 2, pp. 143–147, 2004.
- [19] T. S. Li, L. Liu, B. Zhang et al., "Passive behavior of a bulk nanostructured 316L austenitic stainless steel consisting of nanometer-sized grains with embedded nano-twin bundles," *Corrosion Science*, vol. 85, pp. 331–342, 2014.
- [20] C. Pan, L. Liu, Y. Li, S. Wang, and F. Wang, "Passive film growth mechanism of nanocrystalline 304 stainless steel prepared by magnetron sputtering and deep rolling techniques," *Electrochimica Acta*, vol. 56, no. 22, pp. 7740–7748, 2011.



Journal of
Nanotechnology



International Journal of
Corrosion



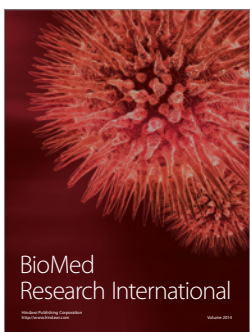
International Journal of
Polymer Science



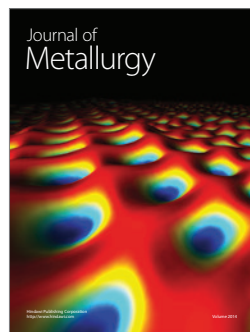
Smart Materials
Research



Journal of
Composites



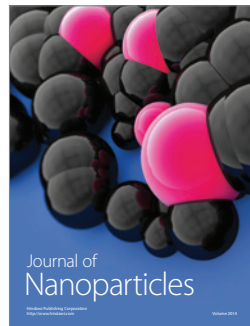
BioMed
Research International



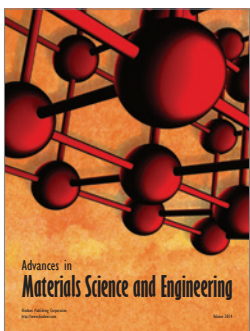
Journal of
Metallurgy



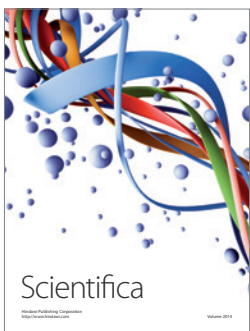
Journal of
Materials



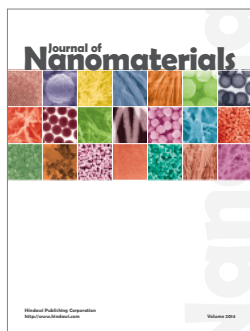
Journal of
Nanoparticles



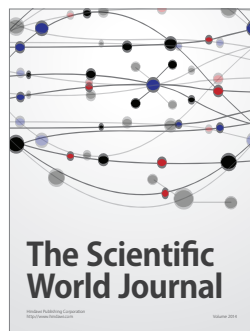
Advances in
Materials Science and Engineering



Scientifica



Journal of
Nanomaterials



The Scientific
World Journal



International Journal of
Biomaterials



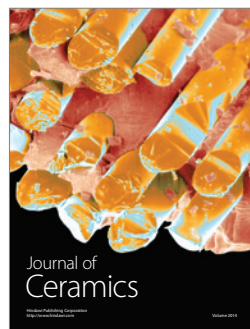
Journal of
Nanoscience



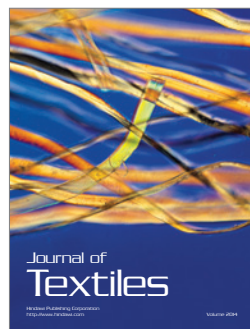
Journal of
Coatings



Journal of
Crystallography



Journal of
Ceramics



Journal of
Textiles